Ultrafast Science
A SCIENCE PARTNER JOURNAL

RESEARCH ARTICLE

Petahertz Polarimetry Using Tunneling Ionization

Danylo T. Matselyukh[1,2,3], Wosik Cho[1,2], Bin Kim[1,2], Gian Müller[3], Hans Jakob Wörner[3], and Kyung Taec Kim[1,2*]

[1]Center for Relativistic Laser Science, IBS, Gwangju, Republic of Korea. [2]Department of Physics and Photon Science, GIST, Gwangju, Republic of Korea. [3]Laboratory of Physical Chemistry, ETH Zürich, Zürich, Switzerland.

*Address correspondence to: kyungtaec@gist.ac.kr

Citation: Matselyukh DT, Cho W, Kim B, Müller G, Wörner HJ, Kim KT. Petahertz Polarimetry Using Tunneling Ionization. *Ultrafast Sci.* 2025;5:Article 0113. https://doi.org/10.34133/ultrafastscience.0113

Submitted 16 May 2025
Revised 19 August 2025
Accepted 24 August 2025
Published 7 October 2025

Light–matter interactions are highly dependent on the precise polarization of the light's electric field; accurate characterization of a laser pulse's time-dependent polarization is therefore critical for ultrafast science. Conventional pulse characterization methods, however, have been developed for investigating linearly polarized pulses, and their polarization-sensitive extensions often rely on restrictive iterative reconstruction algorithms. Here, we demonstrate a field-resolved approach allowing the accurate characterization of an ultrashort optical pulse's time-dependent polarization by using tunneling ionization as a polarization-sensitive temporal gate. Two inherently synchronized gating pulses are used to directly probe both orthogonal components of an arbitrarily polarized sample pulse's electric field, allowing the Stokes parameters as well as the 3-dimensional electric field to be determined on a hundred-of-attoseconds timescale. We use the technique to reveal the often-overlooked polarization impurities induced by pulse post-compression and to demonstrate a novel transmissive minimum-dispersion polarization rotator uniquely compatible with few-cycle laser pulses. Because of its excellent sensitivity and temporal resolution, the technique will allow for a better understanding of both technologically relevant processes (such as post-compression, attosecond polarization gating, or all-optical polarization control) and fundamentally important phenomena (electronic properties of chiral molecules, including proteins and DNA).

Introduction

The field of ultrafast science relies entirely on the use of ultrashort laser pulses to study processes that are too fast to be measured directly. Successful and accurate ultrafast experiments require the precise characterization of the electric field $\mathbf{E}(t)$ of the pulses they employ: Otherwise, one risks incorrectly interpreting purely light-induced signals, sometimes called "coherent artifacts" [1], as pump-induced processes.

Over the last 3 decades, many characterization methods have been developed to address this challenge, employing a combination of cross-correlation [2], interferometry [3], and nonlinear frequency mixing (particularly second harmonic generation [4]) to characterize the time evolution of a pulse's electric field. Since the prototypical systems that ultrafast science initially studied were often centro-symmetric or isotropic, most of these methods focused on reconstructing a one-dimensional representation $\mathbf{E}(t) = E_\mathbf{x}(t)\hat{\mathbf{x}}$ of the pulse [5]. As the field matures, the systems of interest become more complex and their interactions with light more nonlinear. Consequently, single-dimensional descriptions of such ultrafast processes often fail, requiring higher-dimensional models and characterization of the laser field.

An important example of this breakdown is the field-driven rescattering of a strong-field ionized electron off its parent atom/molecule [6]. This attosecond-timescale process leads to a variety of phenomena including high harmonic generation (HHG) [7], laser-induced electron diffraction [8], and nonsequential double ionization [9]. All of these—even when the parent is centrosymmetric—are highly sensitive to the precise electric field: For example, the previously listed processes all exhibit a strong dependence on ellipticity [10]. This sensitivity to the field (i.e., the instantaneous polarization) is not only of scientific interest but also technologically relevant, forming the basis of polarization gating—a method for producing attosecond light pulses [11]. A more widely applicable example of the complex interaction of polarization and structured matter is the all-optical switching of light through polarization-sensitive nanoplasmonic interactions [12]: a promising approach toward photonic computing. Bringing it to the desired petahertz regime [13], however, requires the ability to characterize the polarization of light on a sub-femtosecond timescale, a yet unrealized challenge (only sensitivity has been demonstrated thus far [14]).

The study of these technologically relevant structured ultrafast light–matter interactions therefore requires expanding the temporal characterization of the pulse's electric field from a single dimension to the entire polarization plane $\mathbf{E}(t) = E_\mathbf{x}(t)\hat{\mathbf{x}} + E_\mathbf{y}(t)\hat{\mathbf{y}}$. Such a characterization presents many challenges that have been addressed in a variety of ways.

In cases where the electric field along 2 orthogonal polarization axes is entirely spectrally overlapped, the combination of a single linearly polarized ultrashort pulse characterization with multiple interferometric measurements can be sufficient for the reconstruction of the entire electric field of the pulse [15]. POLLIWOG [16] is the first example of such techniques.

When this spectral overlap is absent, i.e., when certain spectral components are entirely orthogonally polarized, the interferometric approach breaks down. This can be resolved by increasing the number of linearly polarized ultrashort pulse characterizations but then requires overcoming the "phase problem": Since the characterizations only measure the intensity of perturbative nonlinear processes, they are insensitive to the phase difference between the multiple measurements.

A tomographic reconstruction step is therefore necessary, requiring 3 or more individual ultrafast measurements in different polarization planes and a subsequent global phase retrieval. The techniques TURTLE [17] and D-TURTLE [18] fall into this category. While successful at retrieving the intensity and phase of a laser pulse in the polarization plane, the need for a series of experimental acquisitions, each followed by one-dimensional iterative reconstructions, and then a global tomographic reconstruction makes the methodology slower and somewhat cumbersome to apply.

Some more recent approaches attempt to overcome the need for multiple measurements and reconstructions by simultaneously varying the delay and polarization projection angle during the measurement [19,20]. Only a single iterative reconstruction is then needed to retrieve the pulse's polarization in the time domain. These, however, have yet to be applied to few-cycle pulses (FCPs), as their implementation relies on the use of relatively thick transmissive optics.

When partial spectral overlap is maintained between the orthogonal polarization components, a hybrid tomographic/interferometric approach can be employed, where 2 orthogonal linear pulse characterizations are performed and only the spectrum is measured at intermediate polarization angles. This is used in recent work on polarization-sensitive d-scan [21].

Here, we propose a new approach for the complete temporal characterization of an optical pulse's polarization that entirely avoids the phase problem. Our approach leverages field-resolved metrology (FRM): a set of pulse characterization techniques that use a subcycle gating event to capture the electric field of a pulse in time [22]. FRM encompasses techniques that operate in ambient conditions such as NPS [23], field-induced reflectivity modulation [24], and TIPTOE [25], as well experimentally bulkier techniques (due to their reliance on HHG) such as attosecond streaking [26], AIRES [27], and the petahertz oscilloscope [28]. Of these, we expand on tunneling ionization with a perturbation for the time-domain observation of an electric field (TIPTOE), due to its unique sensitivity to polarization (demonstrated below) and ease of implementation.

TIPTOE measures the electric field of a sample laser pulse $\mathbf{E}$ by taking advantage of the highly nonlinear processes of strong-field ionization (SFI) to create a sub-femtosecond gating event [29]. A TIPTOE measurement scans an intense gating laser pulse $\mathbf{E}_G$ with respect to a sample pulse $\mathbf{E}$ in time t and records the modulation of the SFI yield in ambient air $N_{\mathrm{sig}}(t)$ (see Fig. 1A). In the few-cycle limit, the linear interference of the most intense half-cycle of the gating pulse $\mathbf{E}_{\mathrm{G,max}}$ with the sample pulse $\mathbf{E}(t)$ leads to a modulation in the maximum intensity $\mathbf{E}_T(t) = \mathbf{E}(t) + \mathbf{E}_{\mathrm{G,max}}$, and therefore, the probability of SFI $P(t)$ maps $\mathbf{E}(t)$ up to a shift in carrier envelope phase (CEP). Since the total electric field strength $|\mathbf{E}_T(t)|$ is only significantly affected by the component of the signal electric field that is parallel to the polarization of the gate pulse $|\mathbf{E}_T(t)| \simeq |\mathbf{E}_{\mathrm{G,max}}| + \mathbf{E}_{\parallel}(t)$ (see Fig. 2A), TIPTOE is directly sensitive to the polarization of the signal. Specifically, TIPTOE measures a projection of the signal electric field $\mathbf{E}$ along $\mathbf{E}_{\mathrm{G,max}}$ [30].

In this work, we have used this sensitivity of TIPTOE to polarization to measure the time evolution of the 2-dimensional electric field of an arbitrary pulse. Because of the unique phase sensitivity of FRM, 2 orthogonal projections of the sample electric field can be directly combined, revealing the full evolution of the pulse's electric field and therefore its polarization as a function of time.

Results and Discussion

Instrument design

Experimentally realizing a polarization-sensitive TIPTOE (PS-TIPTOE) requires the arbitrarily polarized signal pulse of interest $\mathbf{E}(t)$ to be probed with 2 orthogonally polarized gating pulses $\mathbf{E}_{\mathrm{G,x'}} \cdot \mathbf{E}_{\mathrm{G,y'}} = 0$. Other TIPTOE studies [30,31] have taken a similar experimental approach to TURTLE to achieve this: A waveplate has been used to rotate the gate pulse's polarization requiring successive TIPTOE measurements and an achromatic waveplate. This increases the number of experimental steps for a measurement, which increases the device complexity and the duration of the measurement. An important accomplishment of our novel methodology is realizing this double-orthogonal probing of the pulse simultaneously, at the same point, with the same detector, and in ambient conditions. This resolves the previously listed limitations while maintaining a small footprint and only requiring the motorization of a single experimental parameter. Our methodology also ensures that the signal pulse is identical in both probing steps, removing the need for the calibration of multiple detectors.

For both measurements, a regular TIPTOE scheme is used (see Fig. 1A): A variable delay t is introduced between the signal and gating pulses before they are focused colinearly to an intensity of 10^{12} to 10^{13} W cm^{-2} between a pair of biased copper electrodes ($\mathrm{D_{sig}}$). The high intensity creates ions through SFI, which are collected by the electrodes and recorded through a charge amplifier circuit [29], yielding the signal SFI yield $N_{\mathrm{sig}}(t)$. The gate pulse is separately refocused between a second pair of electrodes ($\mathrm{D_{ref}}$) to produce a reference SFI yield $N_{\mathrm{ref}}(t)$.

Unlike the more well-established experimental realization of in-line TIPTOE, which uses a concentric double mirror [29] to split, delay, and recombine the signal and gate pulses, the novel instrument uses a Mach–Zehnder-like interferometric design. The gate pulse is split from the signal through a low-angle-of-incidence reflection off an uncoated glass wedge pair (WP). These WPs are often found in attosecond beamlines, allowing the PS-TIPTOE design (like d-scan) to be easily incorporated into existing experiments. The variable delay t is introduced using a closed-loop linear piezoelectric actuator (P-622.1CD, Physik Instrumente), which can be placed under any low-angle-of-incidence optic (such as M3 and CCM1). The signal and gate pulses are then collinearly recombined at a holey

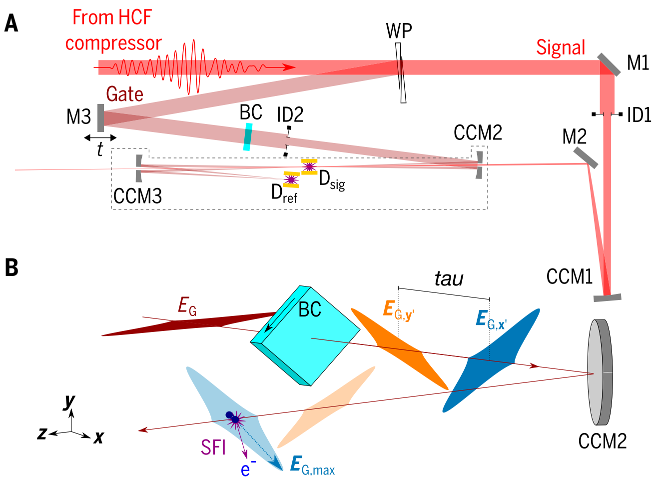

Fig. 1. PS-TIPTOE design. (A) Optical design of PS-TIPTOE. Flat mirrors are labeled M*, while concave mirrors are labeled CCM*. Other acronyms are defined in the main text. After PS-TIPTOE has been performed, the optics within the dashed box can be easily removed, allowing for other attosecond experiments to be performed with a well-characterized pulse. (B) Illustration of how the 2 orthogonal gate pulses are created with the BC. An arrow on the crystal illustrates the orientation of the fast axis.

mirror (CCM2). The gate is reflected and focused by the silver-coated concave surface while the signal passes through the hole.

Although this interferometric design is more susceptible to instabilities in the delay, it allows for the signal and gate to be manipulated separately, which is critical to the creation of the orthogonally polarized gate pulses. Furthermore, it allows for the intensity of the signal and gate pulses to be independently and continuously adjusted, something that is difficult to do with in-line TIPTOE. Fine intensity modulation is achieved with the help of 2 iris diaphragms (ID1 and ID2), while coarse adjustments are made by changing the curvature of the focusing mirrors (CCM1 and CCM2). In the results shown in this work, where the combined gate-pulse energy was 500 nJ, a gate focal length of 150 mm was used. Once the TIPTOE signal was optimized, the gate focal spot full width at half maximum (FWHM) was found to be 26 μm.

While the electrodes are adjusted to be at the focus of the gate beam, the focus of the signal beam can be set much further downstream, allowing an entirely separate experiment to be performed at the signal's focus. In this way, the PS-TIPTOE device can be used to characterize sub-micro- to multi-millijoule laser pulses (low-GW–TW peak power). For a total input energy of 20 μJ, a 500-mm focal length mirror was employed to loosely focus the signal. In such a configuration, the laser fluence of the signal pulse was found to be 10 times lower than each of the gate pulses' at their focus.

Once PS-TIPTOE is complete, the 2 holey mirrors and the electrodes can be removed, ID1 can be opened, and an attosecond experiment can be performed with the fully characterized beam.

As in [31], performing the experiment on the far field of the signal pulse allows the transverse structure of the pulse to be investigated. This is achieved by tuning the alignment of CCM1 or M2 such that the gate focus interrogates different parts of the signal beam. While we have been able to observe differences in the transverse spatial distribution of the spectrum, combining multiple measurements to reconstruct the pulse's phase front is still out of reach.

Performing the 2 orthogonal TIPTOE measurements at the same point and with the same detector removes difficulties associated with duplicating the signal pulse and calibrating the relative sensitivity of multiple detectors. It does, however, require the 2 signals to be separated in some way. We achieve this in the time domain: A known constant delay τ is introduced between the 2 orthogonal gating pulses. As a result, a single sweep over a large enough t range captures the TIPTOE measurements of both polarization components.

Similar to [15], this delay τ is introduced by passing a single FCP through a thick birefringence crystal (BC). Details on the crystal are given in the materials and methods section. As shown in Fig. 1B, placing the fast axis of the BC at 45° with respect to the polarization axis of the pulse (the exact procedure for this can be found in the subsection titles "Initialization procedure") splits it into a pair of orthogonally polarized pulses with a delay τ determined by the path length through the crystal, its birefringence, and the exact spectrum of the FCP. In the absence of cross-phase modulation inside the BC, the fast and slow axes each act as their own polarizer, removing the need for a separate polarizer in the gate arm. Moreover, it is not even necessary for the initial FCP to be linearly polarized; even a circularly polarized input pulse yields 2 linearly polarized gate FCPs. This allows the gating pulse to be created directly from the output of the nonlinear post-compression.

Operation and calibration

In addition to the fixed delay τ, a nonzero CEP difference $\Delta\phi_0$ also exists between the 2 gate pulses. While the delay separates the orthogonal signals in time, the CEP difference induces a CEP shift in the measured signals (we show this analytically in the subsection "Derivation of PS-TIPTOE yield"). Reconstructing the full electric field of the signal pulse requires us to directly recombine the 2 orthogonal projections of the pulse and therefore to correct for the effect of both the delay and the CEP difference. We achieve this by performing a calibration measurement with a well-known signal pulse: one with a well-defined polarization. To do this, a broadband wire-grid polarizer (WP25L-UB, Thorlabs) is introduced just before the recombination mirror such that the signal pulse is entirely horizontally polarized.

A TIPTOE measurement is then performed: The single-laser-shot SFI yields ,$N_{sig}(t)$ and ,$N_{ref}(t)$ are recorded while the delay t is swept continuously using the piezoelectric stage. Each delay is only recorded once per sweep, with each measurement consisting of multiple sweeps. The measurements presented here contain 5 sweeps, covering a total delay range of 800 fs with 80-as steps. At the laser's 1-kHz repetition rate (see subsection "Laser system" for additional details on the laser system), each sweep takes 10 s to perform, with the total measurement being completed in under a minute. The result of the calibration measurement is shown in Fig. 2.

Pre-processing of the TIPTOE trace includes correcting for long-term drifts in delay t and laser intensity fluctuations. The drift is corrected by shifting the delay of each sweep to maximize the cross-correlations between them; these normally fall within a range of a few-hundred attoseconds. No further corrections for delay instabilities were found to be necessary. Laser intensity fluctuations are corrected by fitting a second-order polynomial to the signal N_{sig} versus reference N_{ref} SFI yields for temporal ranges that do not exhibit a signal. The resulting

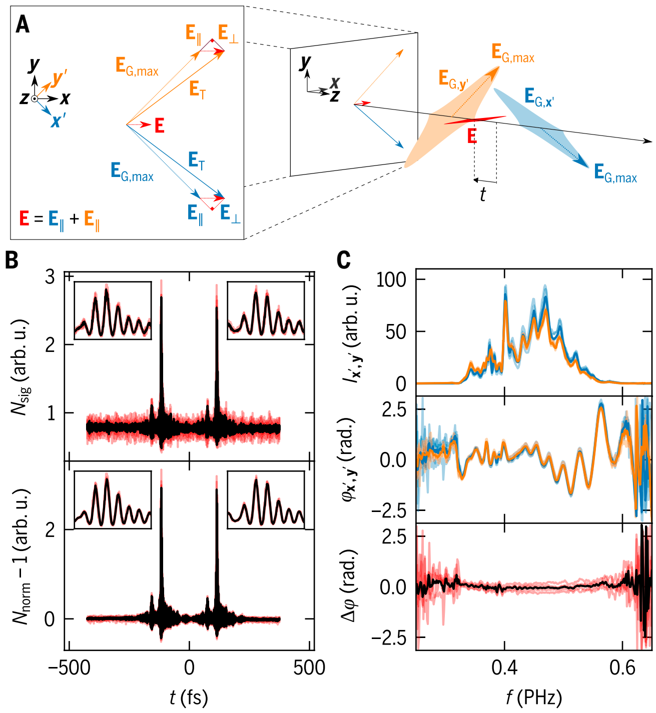

Fig. 2. Calibration of PS-TIPTOE. (A) Schematic of pulse structure in the time domain and a vector plot demonstrating the polarization sensitivity of the TIPTOE process. A weak sample field (red) can be reconstructed through its perturbation of 2 stronger orthogonal fields (orange and blue). (B) Raw results of a PS-TIPTOE measurement on a few-cycle linearly polarized pulse in the time domain. Each sweep is plotted in semitransparent red, and the measurement mean in black. (C) Fourier analysis of the "raw" electric field $E_{\mathbf{x}',\mathbf{y}'}$ (split at $t = 6$ fs into 2 parts). The results from the first part $E_{\mathbf{x}'}$ are plotted in blue, and the second part $E_{\mathbf{y}'}$ in orange. For the 2 parts, each sweep is semitransparent, while the mean is solid in color.

polynomial is used to subtract the reference fluctuations from the signal and normalize the latter yielding N_{norm}.

The 2 components of the electric field can be extracted from the SFI yield using the following expression (derivation presented in subsection "Derivation of PS-TIPTOE yield"):

$$N_{\text{norm}}(t) - 1 \propto \Re\left(E_{\mathbf{x}'}(t) + E_{\mathbf{y}'}(t+\tau)e^{i\Delta\phi_0}\right) + O\left(E^2\right). \quad (1)$$

In our derivation of Eq. (1), we assume that SFI from one gate pulse has negligible temporal overlap with the electric field of the other, and that this SFI's temporal structure can be approximated as a delta function. The former would only be of concern if the gate pulse delay was on the order of the pulse length, while the latter has been well established in previous work [29,32]. Reconstruction schemes [32,33] could replace this expression when characterizing longer pulses or when higher accuracy is desired.

Splitting $N_{\text{norm}}(t) - 1$ at a delay of 6 fs separates the $E_{\mathbf{x}'}$ and $E_{\mathbf{y}'}$ contributions, and performing Fourier analysis on the resulting halves (see Fig. 2C) removes the nonfundamental-frequency contributions $O\left(E^2\right)$, allowing us to observe the 2 orthogonal electric field components in the frequency domain. For longer signal pulses, it may be advantageous to separate the 2 components in a more sophisticated manner; however, this was not found to be necessary in this work on few-femtosecond pulses. As the calibration pulse is linearly polarized, $\left|E_{\mathbf{x}'}\right|^2 = I_{\mathbf{x}'}$ and $\left|E_{\mathbf{y}'}e^{i\Delta\phi_0}\right|^2 = I_{\mathbf{y}'}$ are almost identical, even when comparing individual sweeps (this similarity allows the dynamic range of the technique to be estimated: see Estimate of dynamic range).

To compare the spectral phases ϕ, we unwrap and then subtract the group delay (evaluated by finding the mean gradient over the spectrum: $\tau_{\mathbf{x}'} = -119.80$ fs, $\tau_{\mathbf{y}'} = 113.87$ fs) from each half. The remaining average phase difference ($\Delta\overline{\phi} = -2.08$) is then also subtracted. The resulting "centered" spectral phases $\phi(f) = \arg(E(f))$ are found to be almost identical, demonstrating that—although originating from orthogonal TIPTOE measurements—the 2 halves observe the same pulse. From this, it is evident that the subtracted quantities are the 2 desired calibration quantities $\tau = \tau_{\mathbf{y}'} - \tau_{\mathbf{x}'} = 231.66$ fs and $\Delta\phi_0 = \left(\Delta\overline{\phi} \bmod 2\pi\right) = -2.08$ Having extracted them from the calibration measurement, they can now be applied to any subsequent measurements to reconstruct the 2-dimensional time-dependent electric field of an arbitrary pulse. If the gating were to be performed with longer and less intense pulses, the response function of the 2 gates may be sufficiently different that higher-order spectral phase terms may need to be compensated. This was, however, not found to be necessary with the hundred-nanojoule few-cycle pulses employed in our work.

Petahertz polarimetry

Having calibrated the PS-TIPTOE instrument, we replace the polarizer with an equally thick piece of fused silica and repeat the TIPTOE measurement. In this way, we observe the "unconditioned" output of the laser system. Due to the cascading nonlinear processes occurring during the nonlinear broadening, we expect this to have nonnegligible vertical polarization components, orthogonal to the major polarization axis (MPA).

The results of this PS-TIPTOE measurement are presented as 2 independent orthogonal fields (Fig. 3A) and converted into spectrally resolved Stokes parameters [34,35] (see Fig. 3B; subsection "Calculation of Stokes parameters" describes how these are obtained). Specifically, we employ S_0 (the Stokes intensity parameter), ψ (the major axis angle in the laboratory frame where 0° corresponds to the horizontal), and S_3 / S_0 (the degree of circularity).

The measurements show that the laser system's output is not entirely linearly polarized (separately confirmed using a Glan–Taylor polarizer and a grating spectrometer). Around the frequency of the titanium–sapphire laser (0.35 to 0.4 PHz), we see abrupt fluctuations in the polarization parameters as well as an overall approximately quadratic variation in ψ and S_3. Additionally, the parameters exhibit modulations that are very reminiscent of the group dispersion delay (GDD) curves of the chirped mirrors: The phase difference between the s- and p-reflections in the chirped mirror compressor is also affecting its output. Such a measurement demonstrates the importance of characterizing the full electric field, including all polarization components, of a post-compressed pulse.

To verify the accuracy of our device, we also study a linear interaction that is straightforward to model: the effect of an ultrathin free-standing true-zero-order half-waveplate designed for 700-nm light (WPS03-H-700, Newlight Photonics) on the polarization of the signal pulse. To do this, we insert the waveplate where the wire-grid polarizer previously stood and perform multiple measurements while rotating the waveplate fast axis from being aligned along the polarization of

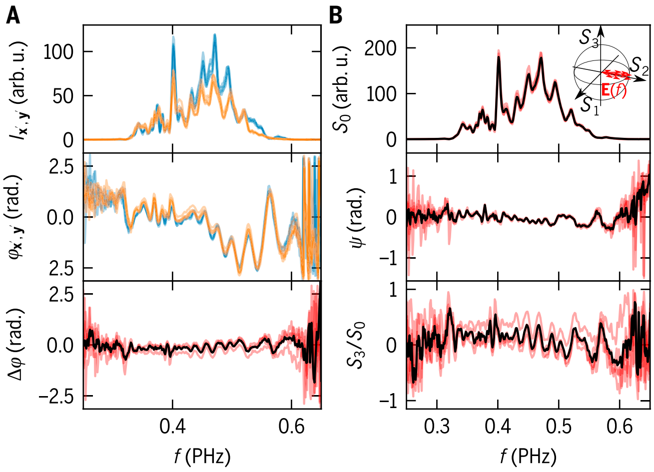

Fig. 3. Detecting polarization impurities of a few-cycle pulse. (A) Fourier analysis of orthogonal electric field components of the laser system's output. The group delay and phase difference removed to yield the middle panel are taken from the calibration measurement in Fig. 2B. (B) Spectrally resolved Stokes vectors calculated from the results of the Fourier analysis as described in subsection "Calculation of Stokes parameters". The inset provides a schematic representation of the measured Stokes vectors in the Poincaré sphere.

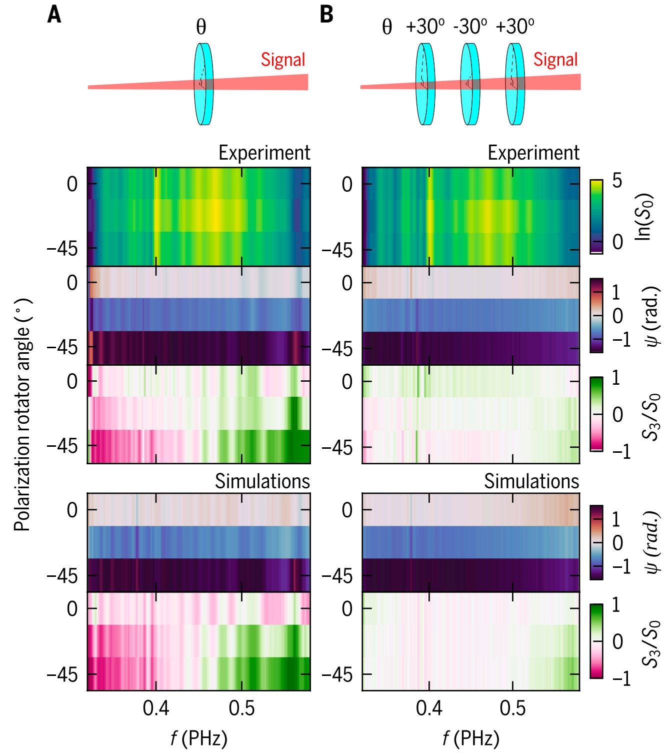

Fig. 4. Measuring deviations in polarization rotation. The effect of rotating a zero-order half-waveplate (A) and a 3-waveplate Pancharatnam stack (B) on the Stokes parameters of the laser system's output (A) and the linearly polarized calibration pulse (B). The top 3 panels present the results of PS-TIPTOE measurements, while the bottom 2 are simulations (see subsection "Simulating the effect of the waveplates" for details).

the input signal pulse (horizontal, 0°)—leaving it unchanged—through to −45°, at which point the effect of the waveplate is maximized.

The results, shown in Fig. 4A, are entirely consistent with Jones calculus simulations of the effects of a quartz half-waveplate (bottom panels of Fig. 4). Close to the design wavelength of 700 nm (0.43 PHz), the linear polarization purity is maintained and rotated by twice the angle of the waveplate. For wavelengths shorter than 700 nm, the retardance applied by the waveplate is larger than π, resulting in those wavelengths becoming partially circularly polarized upon transmission. This becomes most pronounced at a wavelength of 480 nm (0.62 PHz), at which the retardance is $3\pi/2$, resulting in a high degree of circularity $S_3/S_0 \approx -1$ and a large uncertainty in ψ. Similarly, for wavelengths longer than 700 nm, the retardance is smaller than π, resulting in the opposite handedness of circular polarization being generated. The fact that the PS-TIPTOE results exhibit opposites signs of S_3 (and therefore handedness) in excellent agreement with the simulations demonstrates its excellent polarization sensitivity.

Characterizing a broadband polarization rotator

Finally, we use our PS-TIPTOE technique to evaluate the performance of a broadband polarization rotator. Our device allows for the polarization ellipse of an FCP to be rotated without introducing considerable GDD, as is the case for commercially available super-achromatic waveplates. The polarization rotator uses the Pancharatnam waveplate stack methodology [36]. It combines 3 ultra-thin free-standing true-zero-order half-waveplates in line with the middle waveplate's fast axis aligned at 60° with respect to the other 2 to produce a minimum-dispersion achromatic waveplate. This results in a polarization rotator with total quartz thickness of only 120 μm, compared to the multi-millimeter-thick commercial achromatic waveplates, which maintains the few-femtosecond pulse length of FCPs.

The performance of the achromatic polarization rotator is tested in the same way as the single waveplate, with the results shown in Fig. 4B. For these measurements, it was necessary to reintroduce the wire-grid polarizer to better demonstrate the degree to which the polarization purity is maintained. The difference between the single waveplate and the stack is immediately evident: The polarization of the pulse is swept across all possible orientations, while its degree of circularity is consistently kept at a minimum across the entire spectrum. Meanwhile, the temporal structure of the FCP is minimally affected: The FWHM increases from 4.4 fs to 5.6 fs after the polarization rotator's introduction. To our knowledge, this is the first time such an achromatic few-cycle polarization rotator has been demonstrated using ultra-thin true-zero-order waveplates.

While we have thus far presented the results of the PS-TIPTOE in the frequency domain (as this is the convention for ultrafast pulse characterization), they can also be examined as a function of time. In fact, because PS-TIPTOE is a form of FRM, the temporal domain is more representative of the experimental results.

The time-dependent electric field is obtained by converting the measured PS-TIPTOE traces into temporal phasors $E_1'(t)$ and $E_2'(t)$ by performing an inverse Fourier transform on the calibrated electric field projections $E_1(f)$ and $E_2(f)$). The time-resolved Stokes vectors $S_n(t)$ are then obtained from $E_1'(t)$ and $E_2'(t)$ in the same way as in the frequency domain (see subsection "Calculation of Stokes parameters" for details). This leads to Fig. 5, which compares the laser system's output, the calibration pulse, the transmission through a single half-waveplate at −45°, and an exotically polarized pulse in the temporal domain.

The first 3are as expected: The linearly polarized calibration pulse's ellipticity is negligible ($S_3 \approx 0$) and the instantaneous frequency along the 2 probing directions is almost identical $f_1 = f_2$, while the unconditioned laser output shows a bit more variation. Upon passing the latter through the half-waveplate, most of the pulse is rotated by 45° but a larger variation in the MPA and ellipticity is observed due to the non-achromaticity of the waveplate. As the pulse is slightly positively chirped, it exhibits $S_3 < 0$ at earlier times where $f_1(t) < 0.43$ PHz followed by $S_3 > 0$ later when $f_1(t) > 0.43$ PHz.

The exotically polarized pulse results are more dynamic and demonstrate the unique capabilities of PS-TIPTOE. The pulse is produced by detuning the orientations of the individual waveplates in the Pancharatnam stack to 42°, 33°, and 63° with respect to the x axis, which was found to maximize the variation in $\psi(f)$ across the spectrum. Figure 5 reveals that while the instantaneous ellipticity of the exotic pulse is moderate and always right-hand circularly polarized ($S_3 > 0$), it exhibits a rapid variation in $\psi(t)$, rotating clockwise by almost 180° in only 10 fs.

Conclusion

In this work, we have introduced the first polarization-sensitive form of FRM: PS-TIPTOE. It exploits the phase sensitivity of FRM to remove the need for tomographic retrieval and reveals the entire electric field of the pulse, allowing its Stokes parameters to be revealed as a function of time and frequency. Compared to other polarization-sensitive ultrafast characterization techniques, it is entirely free of iterative reconstruction steps, improving its ease of use and the interpretability of its results.

The novel technique has been used to measure the complex polarization structure of an FCP synthesized through nonlinear post-compression. Because of its high dynamic range, it was possible to even observe weak polarization impurities, often overlooked in attosecond experiments. The ability to probe these impurities directly in the time domain is unique to PS-TIPTOE, and this capability may help uncover the primary phenomenon responsible for these poorly understood polarization perturbations in the future.

Finally, PS-TIPTOE has also been shown to correctly capture the chromatic dependence of a zero-order half-waveplate's retardance and used to demonstrate a novel achromatic

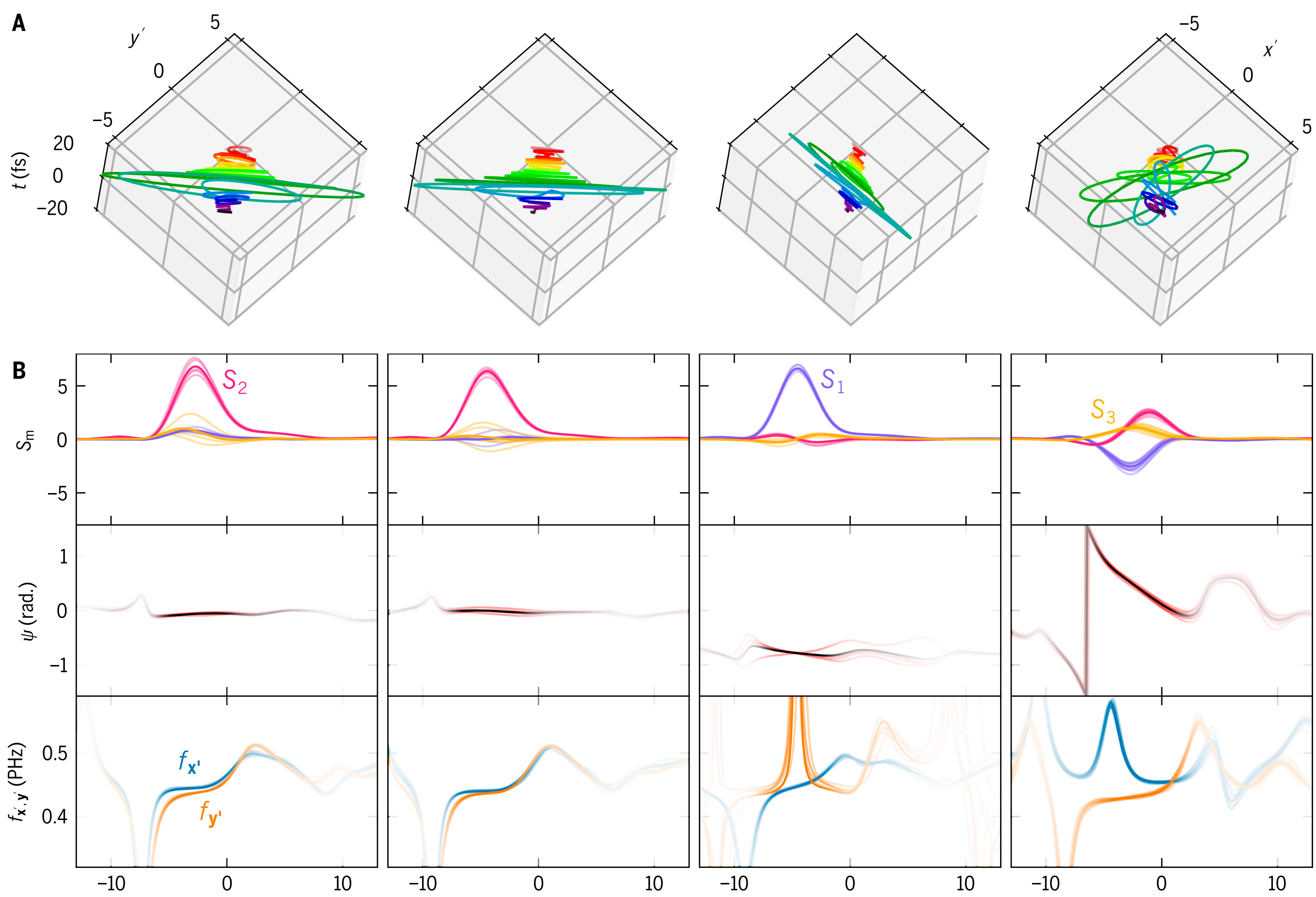

Fig. 5. Sub-femtosecond probing of Stokes parameters. (A) Three-dimensional representation of the measured electric field (up to a shift in CEP) for different signal pulses. (B) Temporally resolved Stokes parameters (S_1, pink; S_2, purple; S_3, orange), major polarization axis ψ, and instantaneous frequency $f(t) = \frac{1}{2\pi}\frac{d\phi}{dt}$ along the orthogonal probing axes **x′** and **y′** of the laser output (first column), the linearly polarized calibration pulse (second column), the effect of a zero-order waveplate −22.5° on it (third column), and an exotically polarized pulse (final column). The shading of ψ and f is proportionate to temporal intensity S_0.

minimum-dispersion polarization rotator that addresses the limitations of a single half-waveplate while preserving the few-femtosecond nature of the FCP.

Materials and Methods

Birefringent crystal

An uncoated a-cut 0.5-mm-thick α-BBO (α-phase barium borate, α-BaB_2O_4, Newlight Photonics) crystal was used to create the orthogonal gating pulse pair. α-BBO was chosen due to its high overall birefringence, but lower birefringence in group velocity dispersion (GVD) compared to calcite. Similarly, the a-cut maximizes the birefringence while minimizing the overall GDD introduced. Upon passage through the crystal, a ~200-fs delay is introduced between the orthogonal pair of gating pulses. The GDD introduced into the gate pulses by the α-BBO can be balanced by the adjustable fused silica WP in the signal beam. The total thickness of fused silica necessary to match the average GDD of the 0.5-mm-thick α-BBO is approximately 1 mm.

Since the fast and slow axes of the BC each yield their own linearly polarized pulse, it can be used to produce an orthogonal pulse pair from any pulse that exhibits approximately unimodal temporal intensity profiles for 2 orthogonal projections. Pulses that are locally linearly polarized but whose polarization oscillates over time, sometimes referred to as "twisted polarization", do not satisfy this condition and cannot be characterized with PS-TIPTOE. To the extent of our knowledge, they are very difficult to produce [37,38], especially with few-cycle pulses. Moreover, the unimodal restriction is one that all field-resolved measurements share, making such polarization-twisted pulses incompatible with most attosecond experiments and characterization techniques.

Initialization procedure

Because of the independent tunability of the 2 arms offered by the interferometric design, preparing the PS-TIPTOE instrument for operation is more involved than for the in-line variant. The main goal of this initialization procedure is to ensure that the orthogonal gate pulses are of similar duration and exhibit equal SFI yields: Such a configuration provides the highest-quality measurement of an arbitrary signal pulse.

Initialization is complicated by the difference in GDD of the 2 orthogonal gate pulses—resulting from the different GVD of the fast and slow axes. This difference in GDD makes it impossible for the 2 gate pulses to be simultaneously maximally compressed, which convolves the optimization of the external wedges and the BC's fast axis orientation. To resolve this, we follow the following procedure.

To compress the pulses equally, we take the SFI yield when the fast/slow axis of the BC is set parallel to the input FCP's polarization to be a measure of the compression of the first/second gate pulse. Hence, the first step is to adjust the external compression wedges such that the SFI yield in these 2 extreme configurations of the BC orientation is equal. When this is done correctly, the GDD of the 2 birefringent pulses is approximately equal in magnitude but opposite in sign.

Once the external wedge position is set, the angle of the BC is adjusted such that the total SFI yield is minimized. This step exploits the highly nonlinear nature of SFI to find an optimal angle that simultaneously minimizes both gate pulse's peak intensity and therefore ensures that they are equally intense. As a result, the gate pulses are polarized at 45° with respect to the horizontal axis of the laboratory frame (see Fig. 1B).

When using an approximately linearly polarized gate pulse, as is the case in this work, it is very easy to convert the PS-TIPTOE into a conventional TIPTOE. This is done by aligning either the slow or the fast axis of the BC with input pulse's polarization, yielding a single linearly polarized gate pulse (used for the regular TIPTOE measurement) and a delayed/advanced pedestal containing the polarization impurities, which have no effect on the recorded TIPTOE trace. Rotating the BC seamlessly transitions the PS-TIPTOE device into a TIPTOE device, allowing the user to easily verify that higher-order cross-polarization interactions are negligible for the measured PS-TIPTOE traces.

Laser system

We shall also briefly describe the laser setup employed in this work (omitted from Fig. 1A). A FEMTOPOWER X PRO CEP (FEMTOLASERS Produktions GmbH) titanium–sapphire laser system was used to produced sub-25-fs, multi-millijoule laser pulses centered at 800 nm at a 1-kHz repetition rate. The CEP of the pulse train was stabilized on a few-second timescale using the feed-forward CEP4 module. Long-term stabilization was not employed in this work to ensure that the methodology was compatible with non-CEP-stabilized laser systems. To create the FCP, 1.5 mJ of pulse energy was focused into a 2-m-long 450-μm-diameter stretched hollow-core fiber (HCF) operated in a differentially pumped mode. Nonlinear effects at the entrance to the fiber were minimized by evacuating the entrance chamber using a roughing vacuum pump, while the fiber's exit chamber was filled with 2,000 torr of neon gas. The total transmission efficiency was 60%, yielding a 0.9-mJ spectrally broadened pulse. This was temporally compressed using PC-37_4 broadband chirped mirrors and a pair of adjustable anti-reflection-coated fused silica wedges. The wedges were included to allow the dispersion of the gate pulses to be fine-tuned but are unnecessary for the implementation of PS-TIPTOE. A quarter waveplate was introduced before the HCF to partially compensate for polarization impurities in the laser system output, thereby improving the polarization purity of the broadened FCP. Its angle was optimized by minimizing the reflection off of a Brewster window situated downstream of the HCF.

Estimate of dynamic range

The calibration measurement allows us to estimate the dynamic range of the TIPTOE device. Using the high- and low-frequency tails of the spectrum visible in Fig. 2B, we can evaluate where the phase difference $\Delta\phi(f)$ begins to diverge between the individual sweeps. This occurs when the intensity drops below 1 arbitrary unit ($0.323 > f > 0.591$ PHz). Since the maximum spectral intensity observed is 100 arbitrary units, this translates to an intensity dynamic range of 100 for a single sweep.

We specify the dynamic range of the device, rather than an absolute sensitivity, because of the ease with which the intensity of the signal and gate pulses can be adjusted. As the device operates with pulse energies in the microjoule range, the input energy must often be considerably attenuated when using it with high-power laser systems. This ensures that a user can always adjust the intensity to achieve sufficient signal. In such a situation, the dynamic range is a more relevant measure of the device performance.

Calculation of Stokes parameters

The Stokes parameters are evaluated by taking the 2 projections of the signal pulse measured using PS-TIPTOE (after applying the calibration) E_1 and E_2 to be orthogonal measurements in a fixed basis. More precisely, they are measurements of the electric field along $\mathbf{x'}$ and $\mathbf{y'}$—axes that are rotated −45° with respect to the x and y axes. The rotation arises from the manner in which we calibrate the instrument: Since the calibration pulse is taken to be horizontally polarized, the horizontal x axis must lie between the axes that we measure.

This is almost equivalent to the treatment of polarization adopted in Jones calculus (apart from the additional rotation). We can therefore employ the already developed machinery for converting between the Stokes and Jones vectors to determine the Stokes parameters. These are as follows:

$$S_0 = \left|E_{\mathbf{x'}}\right|^2 + \left|E_{\mathbf{y'}}\right|^2 \tag{2}$$

$$S_1 = \left|E_{\mathbf{x'}}\right|^2 - \left|E_{\mathbf{y'}}\right|^2 \tag{3}$$

$$S_2 = 2\Re\left(E_{\mathbf{x'}}{}^{*}E_{\mathbf{y'}}\right) = 2\Re\left(E_{\mathbf{x'}}E_{\mathbf{y'}}{}^{*}\right) \tag{4}$$

$$S_3 = 2\Im\left(E_{\mathbf{x'}}{}^{*}E_{\mathbf{y'}}\right) = -2\Im\left(E_{\mathbf{x'}}E_{\mathbf{y'}}{}^{*}\right) \tag{5}$$

A positive value of S_3 corresponds to right-hand/clockwise polarized light (from the point of view of the receiver)

The assignment of the first/second half of the trace to $E_{\mathbf{x'}}$ versus $E_{\mathbf{y'}}$ is determined by the orientation of the birefringent plate. It can be inferred from the waveplate experiments: By comparing the PS-TIPTOE results at a waveplate angle of 0°, −45°, and −90° in the time domain, it is possible to observe which projection is aligned with the fast axis and which with the slow axis as only the latter will exhibit a delay. Specifically, the projection that exhibits a delay at a waveplate angle of −45° must fall along the slow axis and therefore takes the second position in the formulas. When $E_{\mathbf{x'}} = E_{\mathbf{y'}}$, as is the case for the horizontally polarized calibration pulse, then S_2 is positive, $S_0 = S_2$, and $S_1 = S_3 = 0$.

From the Stokes parameters, we can determine the MPA orientation angle with:

$$\psi = \psi' - \frac{\pi}{4} = \frac{1}{2}\arg\left(S_1 + iS_2\right) - \frac{\pi}{4}. \tag{6}$$

The additional factor of $-\frac{\pi}{4}$ rotates the origin of ψ onto the horizontal x axis, i.e., $\psi = 0$ when $S_0 = S_2$. The Stokes vectors presented in Figs. 3 and 4 are calculated using the method described here.

Note that these equations hold for an increasing phase convention, which we have adopted in this work by choosing to analyze the positive Fourier frequencies in Figs. 2 to 4. Working in the decreasing phase convention leaves the first 3 Stokes parameters (S_0, S_1, S_2) unchanged but inverts the last parameter: $S_3(f) \to -S_3(-f)$.

Moreover, once a phase convention is chosen, it is possible to evaluate the Stokes parameters not only in frequency domain but also as a function of time. Applying the inverse Fourier transform to the relevant frequency range (equating to 0.25 to 0.65 PHz in this work) results in time-dependent phasors: $\mathcal{F}^{-1}\left(\left[E_{\mathbf{x'}}(f)\ E_{\mathbf{y'}}(f)\right]\cdot\Pi\right) = E'(t) = \left[E'_{\mathbf{x'}}(t)\ E'_{\mathbf{y'}}(t)\right]$ (here, Π represents the rectangular function that acts as a Fourier filter). These can be used to either reconstruct the full electric field of the measured pulse $\Re\left(E'(t)\right)$ or to evaluate the time-resolved Stokes vectors by inserting the components $E'_{\mathbf{x'}}(t)$ and $E'_{\mathbf{y'}}(t)$ into the equations above. The result of such a time-resolved analysis is presented in Fig. 5.

Simulating the effect of the waveplates

The effect of the waveplates on the polarization of the FCP is simulated using Jones calculus [39]. First, the retardance $\eta(f,l)$ as a function of frequency is calculated from the ordinary and extraordinary refractive indices of quartz [40] (evaluated using the Sellmeier equations). For this, the thickness of the quartz waveplate must be determined. This is taken to be $l = 39$ µm as this yields a retardance of π at 700 nm.

The Jones matrix of the waveplates is then evaluated using the following expression [41]

$$M(\theta,\eta) = e^{-\frac{i\pi}{2}}\begin{bmatrix}\cos^2\theta + e^{i\eta}\sin^2\theta & \left(1-e^{i\eta}\right)\cos\theta\sin\theta \\ \left(1-e^{i\eta}\right)\cos\theta\sin\theta & \sin^2\theta + e^{i\eta}\cos^2\theta\end{bmatrix}, \tag{7}$$

where θ is the angle of the waveplate's fast axis with respect to the horizontal (going anticlockwise from the point of view of the receiver).

The Jones matrix of the Pancharatnam stack polarization rotator is obtained by evaluating the matrix product of the 3 waveplates that it is made up of:

$$M_{\mathrm{P}}(\theta,\eta) = M\left(\theta + \frac{\pi}{6},\eta\right)M\left(\theta - \frac{\pi}{6},\eta\right)M\left(\theta + \frac{\pi}{6},\eta\right). \tag{8}$$

These 2 Jones matrices are then applied to the initial electric field vector $\mathbf{E}^*$. The result of this operation can then be investigated as a function of f as is done in Fig. 6. For the other figures, in the case of the single-waveplate measurement, the initial field is taken to be the output of the HCF compressor (HCF-C). For the Pancharatnam stack, this is taken to be the linearly polarized calibration pulse. Because Jones calculus uses the decreasing phase convention, we must apply the conjugate when constructing the initial field vector from the measured electric field projections: $\mathbf{E}^*(f) = \left[E_{\mathbf{x'}}(f)^*\ E_{\mathbf{y'}}(f)^*\right]$.

The 2components resulting from the matrix operations (ME^* and $M_{\mathrm{P}}E^*$) can then be used in the equations presented in Calculation of Stokes parameters to evaluate the Stokes vectors (being sure to take into account the phase convention when evaluating S_3) after passage through the waveplates. These are presented in the bottom panels of Fig. 4.

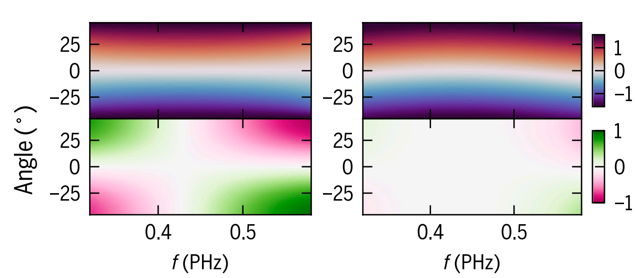

Fig. 6. The effect of a single true-zero-order waveplate and the Pancharatnam stack polarization rotator on linearly polarized light.

Note that one can also determine the waveplates' effect on a perfectly horizontally polarized pulse by taking $\mathbf{E}^* = [1, 1]$.

Derivation of PS-TIPTOE yield

In this section, we shall derive Eq. (21), demonstrating the sensitivity of the technique to polarization and the origin of the calibration quantities in the process.

First, we take the instantaneous probability of SFI to be

$$P(t') = \alpha\left(\left|\mathbf{E}_{G,\mathbf{x}}(t') + \mathbf{E}_{G,\mathbf{y}}(t') + \mathbf{E}(t'+t)\right|^2\right)^n, \quad (9)$$

where α is a constant of proportionality. The total SFI yield is obtained by integrating the instantaneous probability over real time t'. Since the 2 gating pulses are orthogonal, the total PS-TIPTOE yield can then be written as

$$N_{\mathrm{sig}} = \int P(t')\,dt' = \alpha \int \left(\left|\mathbf{E}_{G,\mathbf{x}}\right|^2 + \left|\mathbf{E}_{G,\mathbf{y}}\right|^2 + 2\mathbf{E}_{G,\mathbf{x}}\cdot\mathbf{E} + 2\mathbf{E}_{G,\mathbf{y}}\cdot\mathbf{E} + |\mathbf{E}|^2\right)^n dt'. \quad (10)$$

The experimental design and initialization procedure ensure that

$$\frac{N_0}{2} \approx \int \left|\mathbf{E}_{G,\mathbf{x}}\right|^{2n} dt' \approx \int \left|\mathbf{E}_{G,\mathbf{y}}\right|^{2n} dt' \gg \int |\mathbf{E}|^{2n} dt' \approx 0, \quad (11)$$

which allows Eq. (10) to be expanded and the leading contributions to the yield identified. Due to the highly nonlinear scaling of SFI, these will be terms with the largest powers of $\left|\mathbf{E}_{G,\mathbf{x}}\right|$ and $\left|\mathbf{E}_{G,\mathbf{y}}\right|$. In this expansion, we assume that the SFI induced by one gate pulse does not overlap temporally with the electric field of the other gating pulse, i.e., $\left|\mathbf{E}_{G,\mathbf{x}}\right|^{2n-k}\left|\mathbf{E}_{G,\mathbf{y}}\right|^k = 0$ and $\left|\mathbf{E}_{G,\mathbf{x}}\right|^k\left|\mathbf{E}_{G,\mathbf{y}}\right|^{2n-k} = 0$ for $k = 1, 2$.

Retaining powers of $\left|\mathbf{E}_G\right|^{2n-2}$ and higher, we get:

$$\begin{aligned} N_{\mathrm{sig}} = \alpha \int & \left|\mathbf{E}_{G,\mathbf{x}}\right|^{2n} + n\left|\mathbf{E}_{G,\mathbf{x}}\right|^{2n-2}\left(2\mathbf{E}_{G,\mathbf{x}}\cdot\mathbf{E} + |\mathbf{E}|^2\right) + 2\binom{n}{2}\left|\mathbf{E}_{G,\mathbf{x}}\right|^{2n-4}\left(\mathbf{E}_{G,\mathbf{x}}\cdot\mathbf{E}\right)^2 \\ & + \left|\mathbf{E}_{G,\mathbf{y}}\right|^{2n} + n\left|\mathbf{E}_{G,\mathbf{y}}\right|^{2n-2}\left(2\mathbf{E}_{G,\mathbf{y}}\cdot\mathbf{E} + |\mathbf{E}|^2\right) + 2\binom{n}{2}\left|\mathbf{E}_{G,\mathbf{y}}\right|^{2n-4}\left(\mathbf{E}_{G,\mathbf{y}}\cdot\mathbf{E}\right)^2 \\ & + O(E^3)\ dt'. \end{aligned} \quad (12)$$

Note that this expression holds whether n is an integer or not. In the case of the latter, Newton's generalized binomial theorem can be applied.

We now consider the relationship between the 2 gate pulses $\mathbf{E}_{G,\mathbf{x}} = \Re\left(E_{G,\mathbf{x}}\right)\hat{\mathbf{x}}$ and $\mathbf{E}_{G,\mathbf{y}} = \Re\left(E_{G,\mathbf{y}}\right)\hat{\mathbf{y}}$, which we have now expressed as phasors. One gate pulse is delayed with respect to the other due to the higher refractive index of the BC's slow axis $\Delta n = n_e - n_o$. The additional phase acquired by the delayed gate pulse can be Taylor expanded around the central frequency of the laser pulse f_0':

$$2\pi l \frac{f'}{c}\Delta n(f) = 2\pi l\left(\frac{f_0'}{c}\Delta n(f_0') + \frac{f'-f_0'}{c}\left(\Delta n(f_0') + \dot{\Delta n}(f_0')f_0'\right) + O(f'^2)\right) \quad (13)$$

The first constant term corresponds to the difference in CEP between the gate pulses, while the second linear term to the group delay:

$$\tau = 2\pi l \frac{f'-f_0'}{c}\left(\Delta n(f_0') + \dot{\Delta n}(f_0')f_0'\right) \quad (14)$$

$$\Delta\phi_0 = 2\pi l \frac{f_0'}{c}\Delta n(f_0'). \quad (15)$$

Higher-order terms $O(f^2)$ lead to differences in the dispersion of the pulses, which can influence the relative SFI yields of the 2 gate pulses. Our PS-TIPTOE initialization procedure, however, corrects for this difference. By experimentally setting $\int\left|\mathbf{E}_{G,\mathbf{x}}\right|^{2n}dt' \approx \int\left|\mathbf{E}_{G,\mathbf{y}}\right|^{2n}dt'$, we ensure that the pulses are oppositely chirped, i.e., that $\arg\left(E_{G,\mathbf{y}}(f')\right) - \arg\left(E_{G,\mathbf{x}}(f')\right) \approx \Delta\phi_0 + \tau f'$. Therefore, we can rewrite the expressions for the 2 gating pulses using a common expression for the electric field $\mathbf{E}_G$:

$$\mathbf{E}_{G,\mathbf{x}} = \Re\left(E_G(t')\right)\hat{\mathbf{x}} \quad (16)$$

$$\mathbf{E}_{G,\mathbf{y}} = \Re\left(E_G(\tau - t')e^{i\Delta\phi_0}\right)\hat{\mathbf{y}}. \quad (17)$$

Implementing these expression for the gating pulses back into Eq. (12), we obtain:

$$\begin{aligned} N_{\mathrm{sig}}(t) = N_0 + \alpha \int & 2n\left|\Re\left(E_G(t')\right)\right|^{2n-2}\Re\left(E_G(t')\right)E_{\mathbf{x}}(t'+t) \\ & + 2n\left|\Re\left(E_G(\tau-t')e^{i\Delta\phi_0}\right)\right|^{2n-2}\Re\left(E_G(\tau-t')e^{i\Delta\phi_0}\right)E_{\mathbf{y}}(t'+t) \\ & + O(E^2)\ dt'. \end{aligned} \quad (18)$$

At this point, the expression for the PS-TIPTOE signal has a similar form to what is found in previous work on TIPTOE, with the addition of a few new higher-order terms that originate because the electric fields have been treated as vectors. In these works, the fact that the gating and sample pulses were approximately the same was exploited (together with the convolution theorem) to either fully reconstruct $E(t')$ or to estimate the TIPTOE instrument spectral response function $\mathcal{F}\left(E_G(t')^{2n-1}\right)^*$. Since the similarity between E_G and $E_{\mathbf{x}}$ and $E_{\mathbf{y}}$ is not guaranteed, we must take a slightly different approach.

In the same works, it has been well established that, for close-to-Fourier limited pulse, the instrument response is flat, which is equivalent to approximating $E_G(t')^{2n-1}$ as a delta function. We apply the same approximation, which in our case takes the form:

$$\left|\Re(E_G(t')\right|^{2n-2} = \beta\delta(t') \quad (19)$$

$$\left|\Re(E_G(\tau-t')e^{i\Delta\phi_0}\right|^{2n-2} = \beta\delta(t'-\tau), \quad (20)$$

where β is a scaling factor. Setting $E_G(0) = E_{G,\max}$ to be a real positive number, we find that

$$\frac{N_{\text{sig}}(t)-N_0}{I_0}=N_{\text{norm}}(t)-1=E_{\text{G,max}}\frac{2n\alpha\beta}{N_0}\Re\left(E_{\mathbf{x}}(t)+e^{i\Delta\phi_0}E_{\mathbf{y}}(\tau+t)\right)+O\left(E^2\right). \tag{21}$$

Note that we can safely neglect all terms $O\left(E^2\right)$ as they will not contribute to signals at the carrier frequency f in the Fourier transform of N_{norm}.

Acknowledgments

D.T.M. would like to acknowledge many invaluable discussions with J. Wiese and J. Bredehoeft's insightful proofreading of the manuscript.
Funding: This work was supported by the Institute for Basic Science grant (IBS-R038-D1) and the National Research Foundation of Korea (NRF), grant funded by the Korea government (MIST) (nos. 2022R1A2C3006025 and RS-2023-00303001). D.T.M. would also like to acknowledge support from the NRF Young Researchers' Exchange Programme 2023. D.T.M., G.M., and H.J.W. acknowledge funding from the Swiss National Science Foundation through grant 200020_204928.
Author contributions: D.T.M. and K.T.K. conceived the study. D.T.M., W.C., and B.K. built the few-cycle compressor and the PS-TIPTOE instrument. D.T.M. planned and performed the experiments. D.T.M., G.M., and H.J.W. performed preliminary studies on the minimum-dispersion polarization rotator. D.T.M. analyzed the results. D.T.M. and K.T.K. wrote the manuscript. K.T.K. supervised the study. All authors reviewed the manuscript.
Competing interests: The authors declare that they have no competing interests.

Data Availability

Data underlying the results presented in this paper are not publicly available at this time but may be obtained from the authors upon reasonable request.

Supplementary Materials

Fig. S1

References

1. Dietzek B, Pascher T, Sundstrom V, Yartsev A. Appearance of coherent artifact signals in femtosecond transient absorption spectroscopy in dependence on detector design. *Laser Phys Lett*. 2006;4(1):38–43.
2. Kane DJ, Trebino R. Characterization of arbitrary femtosecond pulses using frequency resolved optical gating. *IEEE J Quantum Electron*. 1993;29(2):571–579.
3. Iaconis C, Walmsley IA. Spectral phase interferometry for direct electric-field reconstruction of ultrashort optical pulses. *Opt Lett*. 1998;23(10):792–794.
4. Miranda M, Arnold CL, Fordell T, Silva F, Alonso B, Weigand R, L'Hiullier A, Crespo H. Characterization of broadband few-cycle laser pulses with the d-scan technique. *Opt Express*. 2012;20(17):18732–18743.
5. Walmsley IA, Wong V. Characterization of the electric field of ultrashort optical pulses. *J Opt Soc Am B*. 1996;13(11):2453–2463.
6. Amini K, Biegert J, Calegari F, Chacón A, Ciappina MF, Dauphin A, Efimov DK, Figueira de Morisson Faria C, Giergiel K, Gniewek P, et al. Symphony on strong field approximation. *Rep Prog Phys*. 2019;82(11):Article 116001.
7. Lewenstein M, Balcou P, Ivanov MY, L'Huillier A, Corkum PB. Theory of high-harmonic generation by low-frequency laser fields. *Phys Rev A*. 1994;49(3):2117.
8. Zuo T, Bandrauk A, Corkum PB. Laser-induced electron diffraction: A new tool for probing ultrafast molecular dynamics. *Chem Phys Lett*. 1996;259(3–4):313–320.
9. L'Huillier A, Lompre L, Mainfray G, Manus C. Multiply charged ions formed by multiphoton absorption processes in the continuum. *Phys Rev Lett*. 1982;48(26):1814.
10. Budil K, Salieres P, L'Huillier A, Ditmire T, Perry M. Influence of ellipticity on harmonic generation. *Phys Rev A*. 1993;48(5):R3437.
11. Sola I, Mével E, Elouga L, Constant E, Strelkov V, Poletto L, Villoresi P, Benedetti E, Caumes JP, Stagira S, et al. Controlling attosecond electron dynamics by phase-stabilized polarization gating. *Nat Phys*. 2006;2:319–322.
12. Wang H, Hu Z, Deng J, Zhang X, Chen J, Li K, Li G. All-optical ultrafast polarization switching with nonlinear plasmonic metasurfaces. *Sci Adv*. 2024;10(8):eadk3882.
13. Heide C, Keathley PD, Kling MF. Petahertz electronics. *Nat Rev Phys*. 2024;6:648–662.
14. Blöchl J, Schötz J, Maliakkal A, Šreibere N, Wang Z, Rosenberger P, Hommelhoff P, Staudte A, Corkum PB, Bergues B, et al. Spatiotemporal sampling of near-petahertz vortex fields. *Optica*. 2022;9(7):755–761.
15. Alonso B, Sola I. Measurement of ultrashort vector pulses from polarization gates by in-line, single-channel spectral interferometry. *IEEE J Sel Top Quantum Electron*. 2019;25(4):1–7.
16. Walecki W, Fittinghoff DN, Smirl AL, Trebino R. Characterization of the polarization state of weak ultrashort coherent signals by dual-channel spectral interferometry. *Opt Lett*. 1997;22(2):81–83.
17. Schlup P, Masihzadeh O, Xu L, Trebino R, Bartels RA. Tomographic retrieval of the polarization state of an ultrafast laser pulse. *Opt Lett*. 2008;33(3):267–269.
18. Perez-Benito O, Weigand R. Characterization of the polarization state of few-cycle laser ´ pulses using d-scan: D-TURTLE. *Opt Laser Technol*. 2024;179:Article 111273.
19. Haham GI, Levin A, Sidorenko P, Lerner G, Cohen O. V-FROG—Single-scan vectorial FROG. *J Phys Photonics*. 2021;3(3):Article 034017.
20. Barbero C, Alonso B, Sola IJ. Characterization of ultrashort vector pulses from a single amplitude swing measurement. *Opt Express*. 2024;32(7):10862–10873.
21. Rivas DD, Raab AK, Guo C, Viotti AL, Sytcevich I, L'Huillier A, Arnold C. Measurement of ultrashort laser pulses with a time dependent polarization state using the d-scan technique. *J Phys Photonics*. 2024;6(1):Article 015003.
22. Herbst A, Scheffter K, Bidhendi M, Kieker M, Srivastava A, Fattahi H. Recent advances in petahertz electric field sampling. *J Phys B Atomic Mol Phys*. 2022;55(17):Article 172001.
23. Sederberg S, Zimin D, Keiber S, Siegrist F, Wismer MS, Yakovlev VS, Floss I, Lemell C, Burgdörfer J, Schultze M, et al. Attosecond optoelectronic field measurement in solids. *Nat Commun*. 2020;11(1):Article 430.

24. Hui D, Alqattan H, Yamada S, Pervak V, Yabana K, Hassan MT. Attosecond electron motion control in dielectric. *Nat Photonics*. 2022;16(1):33–37.
25. Park SB, Kim K, Cho W, Hwang SI, Ivanov I, Nam CH, Kim KT. Direct sampling of a light wave in air. *Optica*. 2018;5(4):402–408.
26. Itatani J, Quéré F, Yudin GL, Ivanov MY, Krausz F, Corkum PB. Attosecond streak camera. *Phys Rev Lett*. 2002;88(17): Article 173903.
27. Wyatt AS, Witting T, Schiavi A, Fabris D, Matia-Hernando P, Walmsley IA, Marangos JP, Tisch JW. Attosecond sampling of arbitrary optical waveforms. *Optica*. 2016;3(3):303–310.
28. Kim KT, Zhang C, Shiner AD, Schmidt BE, Légaré F, Villeneuve DM, Corkum PB. Petahertz optical oscilloscope. *Nat Photonics*. 2013;7(12):958–962.
29. Cho W, Hwang SI, Nam CH, Bionta MR, Lassonde P, Schmidt BE, Ibrahim H, Légaré F, Kim KT. Temporal characterization of femtosecond laser pulses using tunneling ionization in the UV, visible, and mid-IR ranges. *Sci Rep*. 2019;9:Article 16067.
30. Saito N, Ishii N, Kanai T, Itatani J. All-optical characterization of the two-dimensional waveform and the Gouy phase of an infrared pulse based on plasma fluorescence of gas. *Opt Express*. 2018;26(19):24591–24601.
31. Liu Y, Gholam-Mirzaei S, Khatri D, Truong TC, Journigan TD, Cabello C, Lantigua C, Staudte A, Corkum PB, Chini M. Field-resolved space–time characterization of few cycle structured light pulses. *Optica*. 2024;11(6):846–851.
32. Cho W, Shin J, Kim KT. Reconstruction algorithm for tunneling ionization with a perturbation for the time-domain observation of an electric-field. *Sci Rep*. 2021;11(1): Article 13014.
33. Wiese J, Brupbacher K, Bredehoeft J, Matselyukh DT, Jakob Wörner H. Universal and waveform-resolving dual pulse reconstruction through interferometric strong-field ionization. *Opt Express*. 2024;32(27):48734–48747.
34. Stokes GG. On the composition and resolution of streams of polarized light from different sources. *Trans Cambrid Philos Soc*. 1851;9:Article 399.
35. McMaster WH. Polarization and the Stokes parameters. *Am J Phys*. 1954;22(6):351–362.
36. Pancharatnam S. Achromatic combinations of birefringent plates: Part II. An achromatic quarter-wave plate. In: *Proceedings of the Indian Academy of Sciences-Section A*. Bangalore (India): Indian Academy of Sciences; 1955. p. 137–144.
37. Cao Q, Zheng P, Zhan Q. Vectorial sculpturing of spatiotemporal wavepackets. *APL Photonics*. 2022;7(9): Article 096102.
38. Jiang X, Zhou Z, Min C, Zhang Y, Yuan X. Controllable temporal twisting polarization within an ultrafast laser pulse. *Opt Lett*. 2024;49(21):6225–6228.
39. Jones RC. A new calculus for the treatment of optical systems. I. Description and discussion of the calculus. *J Opt Soc Am*. 1941;31(7):488–493.
40. Ghosh G. Dispersion-equation coefficients for the refractive index and birefringence of calcite and quartz crystals. *Opt Commun*. 1999;163(1-3):95–102.
41. Theocaris PS, Gdoutos EE. *Matrix theory of photoelasticity*. Berlin, Heidelberg: Springer; 1979.

Ultrafast Science
A SCIENCE PARTNER JOURNAL

Petahertz Polarimetry Using Tunneling Ionization

Danylo T. Matselyukh, Wosik Cho, Bin Kim, Gian Müller, Hans Jakob Wörner, and Kyung Taec Kim

Citation: Matselyukh D, Cho W, Kim B, Müller G, Wörner H, Kim K. Petahertz Polarimetry Using Tunneling Ionization. *Ultrafast Sci*. 2025;**5**:0113. DOI: 10.34133/ultrafastscience.0113

Light–matter interactions are highly dependent on the precise polarization of the light's electric field; accurate characterization of a laser pulse's time-dependent polarization is therefore critical for ultrafast science. Conventional pulse characterization methods, however, have been developed for investigating linearly polarized pulses, and their polarization-sensitive extensions often rely on restrictive iterative reconstruction algorithms. Here, we demonstrate a field-resolved approach allowing the accurate characterization of an ultrashort optical pulse's time-dependent polarization by using tunneling ionization as a polarization-sensitive temporal gate. Two inherently synchronized gating pulses are used to directly probe both orthogonal components of an arbitrarily polarized sample pulse's electric field, allowing the Stokes parameters as well as the 3-dimensional electric field to be determined on a hundred-of-attoseconds timescale. We use the technique to reveal the often-overlooked polarization impurities induced by pulse post-compression and to demonstrate a novel transmissive minimum-dispersion polarization rotator uniquely compatible with few-cycle laser pulses. Because of its excellent sensitivity and temporal resolution, the technique will allow for a better understanding of both technologically relevant processes (such as post-compression, attosecond polarization gating, or all-optical polarization control) and fundamentally important phenomena (electronic properties of chiral molecules, including proteins and DNA).
Image

Ultrafast Science (ISSN 2765-8791) is published by the American Association for the Advancement of Science. 1200 New York Avenue NW, Washington, DC 20005.